Experimental and Computational Multiphase Flow
Vol. 4, No. 3, 2022, 274–290
https://doi.org/10.1007/s42757-020-0101-3

Cahn-Hilliard Navier-Stokes simulations for marine free-surface flows

Niklas Kühl[1] (✉), Michael Hinze[2], Thomas Rung[1]

1. *Institute for Fluid Dynamics and Ship Theory, Hamburg University of Technology, Am Schwarzenberg-Campus 4, D-21075 Hamburg, Germany*
2. *Department of Mathematics, Universität Koblenz-Landau, Campus Koblenz, Universitätsstrasse 1, D-56070 Koblenz, Germany*

Abstract

The paper is devoted to the simulation of maritime two-phase flows of air and water. Emphasis is put on an extension of the classical Volume-of-Fluid (VoF) method by a diffusive contribution derived from a Cahn-Hilliard (CH) model and its benefits for simulating immiscible, incompressible two-phase flows. Such flows are predominantly simulated with implicit VoF schemes, which mostly employ heuristic downwind-biased approximations for the concentration transport to mimic a sharp interface. This strategy introduces a severe time step restriction and requires pseudo time-stepping of steady flows. Our overall goal is a sound description of the free-surface region that alleviates artificial time-step restrictions, supports an efficient and robust upwind-based approximation framework, and inherently includes surface tension effects when needed. The Cahn-Hilliard Navier-Stokes (CH-NS) system is verified for an analytical Couette-flow example and the bubble formation under the influence of surface tension forces. 2D validation examples are concerned with laminar standing waves reaching from gravity to capillary scale as well as a submerged hydrofoil flow. The final application refers to the 3D flow around an experimentally investigated container vessel at fixed floatation for $Re = 1.4 \times 10^7$ and $Fn = 0.26$. Results are compared with data obtained from VoF approaches, supplemented by analytical solutions and measurements. The study indicates the superior efficiency, resharpening capability, and wider predictive realm of the CH-based extension for free-surface flows with a confined spatial range of interface Courant numbers.

Keywords

Cahn-Hilliard Navier-Stokes (CH-NS)
Volume-of-Fluid (VoF)
free-surface flow
quasi-steady simulation
CFL independence

Article History

Received: 11 August 2020
Revised: 24 October 2020
Accepted: 24 November 2020

Research Article

1 Introduction

Many two-phase flows are characterized by immiscible fluids that feature negligible compressibility. A prominent example refers to maritime free-surface flows. Technical applications of such flows are often subjected to large interface deformations, e.g., breaking waves. The accurate simulation of these flows requires a computational model that conserves the mass of each phase whilst preserving a sharp interface. These requirements still pose a challenge in mesh-based computational fluid dynamics.

Engineering two-phase flow simulations mostly refer to either of two *interface-capturing* methods (Ferziger and Perić, 2012): namely the Level-Set method (Osher and Sethian, 1988) and the *Volume-of-Fluid* (VoF) approach (Hirt and Nichols, 1981), which both reconstruct the free surface from an indicator function. The Level-Set method introduced by Osher and Sethian (1988) or Sussman (1994), Sussman et al. (1998) utilizes a signed distance function to characterize the interface by the zero-value iso surface. The continuous distribution of the signed distance simplifies a higher-order discretization of the related transport equation, and the geometry of the interface can be determined with improved accuracy. A drawback of the standard Level-Set method is that it does not guarantee mass conservation. Olsson and Kreiss (2005) as well as Olsson et al. (2007) proposed a mass conservative Level-Set approach based on a smeared Heaviside function which follows a similar idea compared to the diffuse (VoF) interface approach herein. Two-phase applications of the VoF method suggested by Noh and Woodward (1976) and later refined by Hirt and Nichols (1981) usually employ a scalar volume concentration, of a foreground phase to identify the fluid state of each cell. The method is conservative and capable to predict merging and

✉ niklas.kuehl@tuhh.de

rupturing of free surfaces. For immiscible fluids, any mixing of both phases is undesired but numerically difficult to avoid. Different strategies are conceivable to improve interface compression: Geometric reconstruction schemes, e.g. SLIC (Noh and Woodward, 1976), PLIC (Hirt and Nichols, 1981), or LVIRA (Pilliod and Puckett, 2004), and dedicated downwind-biased advection schemes, e.g., CICSAM (Ubbink and Issa, 1999), HRIC (Muzaferija and Peric, 1999), IGDS (Jasak et al., 1999), or BRICS (Wackers et al., 2011). Geometric reconstruction schemes are afflicted with a considerable algorithmic complexity which reduces their popularity. Dedicated advection schemes are slightly heuristic but fairly simple to implement. They maintain an approximately sharp interface subject to sufficiently small time steps. On the downside, they require transient implicit simulations even for steady state problems, e.g., the calm-water resistance of steady cruising ships. To further improve the interface compression, some authors have proposed to add an artificial compression or anti-diffusion term, e.g., So et al. (2011), Heyns et al. (2013). These methods rely on heuristic compression factors and improve the compressiveness at the expense of a reduced numerical stability.

If surface tension effects are negligible, VoF models using dedicated advection schemes are deemed a good compromise between efficiency, accuracy, and conservation properties. An alternative, much less common approach refers to diffuse interface models, often labelled Cahn-Hilliard (CH) models (Cahn and Hilliard, 1958). Here the (ideally sharp) interface is replaced by a (thin) layer where the fluids mix. The approach is able to mimic phase separation and thus promises resharpening features which are attractive for engineering simulations. Although the neglect of surface tension is an acceptable assumption in many engineering problems, it appears that the CH approach incorporates surface tension in a natural way and no additional model, e.g., the Continuum Method (Brackbill et al., 1992; Lafaurie et al., 1994), is required.

There exist a variety of different CH approaches for two fluids, e.g., models governed by fluids with matched densities (labelled as Model H (Hohenberg and Halperin, 1977)), identical viscosities (Boussinesq Fluid (Jacqmin, 1999)), or so-called thermodynamically consistent systems (Lowengrub and Truskinovsky, 1998; Abels et al., 2012), just to name a few. The thermodynamically consistent approach has received attention for energetic reasons, in particular if an inherent divergence-free velocity field is sought. E.g., Khanwale et al. (2020a, 2020b) recently employed an octree-based mesh refinement approach to an adaptive finite-element discretization of the energy-stable formulation, to study canonical test cases like Rayleigh-Taylor instabilities or rising bubbles.

In addition to the different CH variants, different strategies for their coupling with the momentum and continuity equations have been suggested. Further distinctions refer to balancing either the mass or the volume fluxes between both phases (Lowengrub and Truskinovsky, 1998; Ding et al., 2007), the considered baseline conservation equations (Ding et al., 2007; Abels et al., 2012), and the introduction of modifications to ensure thermodynamic consistency (Lowengrub and Truskinovsky, 1998; Abels et al., 2012). The VoF scheme offers a closed system of PDEs, but entails evolved parametrized approximations. On the contrary, three additional physical parameters occur in the CH method. The first and second correspond to the transition length as well as the surface tension coefficient, and the third parameter refers to the mobility that governs the strength of the phase separation process. Combining the CH model with the Navier-Stokes equations, essentially results in an augmented VoF formulation. This inheres a non-linear, diffusive right-hand side of order four, which is zero outside the inter facial region. The non-linear character is beneficial. It supports an accurate computation of surface tension effects when the interface is adequately resolved and the use of stable, upwind-biased advective approximations in under-resolved flow simulations. To this end, a compressive numerical method is suggested for simulations, where the transition length is under-resolved by the numerical grid and surface tension influences cannot be displayed. The latter is based on an automatic adjustment of the mobility parameter. Possible, minimal blurs are bypassed with a non-linear state equation. The resulting system is virtually insensitive for spatial and temporal resolutions aspects.

The remainder of the paper is organized as follows: Section 2 outlines the mathematical model including a brief introduction into the diffuse interface model. The subsequent third section describes the numerical procedure and outlines implementation aspects. Section 4 covers the verification. The determination of the mobility parameter in under-resolved flows is outlined in Section 5. Sections 6.1 and 6.2 validate the CH-approach and the mobility parameter estimation against frequently studied two-dimensional test cases, i.e., standing waves in the capillary and gravity scale as well as a submerged hydrofoil flow. The comparison of results and computational efforts obtained from a CH- and a VoF-approach for a widely used 3D container ship benchmark case is depicted in Section 6.3. Final conclusions are drawn in Section 7. Within the publication, Einstein's summation convention is used for lower-case Latin subscripts. Vectors and tensors are defined with reference to Cartesian coordinates and dimensionless variables are consistently marked with an asterisk.

2 Mathematical model

Following the work of Ding et al. (2007), one can distinguish between mass conservative and volume conservative CH strategies. To illustrate this, we define the specie densities (ρ^a, ρ^b) by a simple linear equation of state, which connects them to their constant bulk densities (ρ_a, ρ_b), i.e., $\rho^a = c\rho_a$ and $\rho^b = (1-c)\rho_b$. The expression $c = V_a / V$ represents the volume concentration of the foreground phase, the respective concentration of the background phase reads $V_b / V = (V - V_a) / V = (1-c)$. The mass conservation of the species a and b are governed by

$$\frac{\partial \rho^a}{\partial t} + \frac{\partial v_i \rho^a}{\partial x_i} = \sigma^a, \quad \frac{\partial \rho^b}{\partial t} + \frac{\partial v_i \rho^b}{\partial x_i} = \sigma^b \tag{1}$$

where σ^a, σ^b denote the mass transfer rates into the species a and b respectively, v_i refers to the velocity, and x_i denotes the spatial Cartesian coordinates. Using $\rho = \rho^a + \rho^b$, an analogue continuity relation is obtained for the mixture:

$$\frac{\partial \rho}{\partial t} + \frac{\partial v_i \rho}{\partial x_i} = \sigma^a + \sigma^b \tag{2}$$

Substituting ρ^a and ρ^b by $c\rho_a$ and $(1-c)\rho_b$, one can reformulate Eq. (1) and obtain

$$\frac{\partial c}{\partial t} + \frac{\partial v_i c}{\partial x_i} = \frac{\sigma^a}{\rho_a}, \quad -\frac{\partial c}{\partial t} - \left(\frac{\partial v_i c}{\partial x_i} - \frac{\partial v_i}{\partial x_i} \right) = \frac{\sigma^b}{\rho_b} \tag{3}$$

Summing up Eq. (3) yields an alternative continuity equation, which describes the volume change:

$$\frac{\partial v_i}{\partial x_i} = \frac{\sigma^a}{\rho^a} + \frac{\sigma^b}{\rho^b} = \frac{\partial}{\partial x_k}\left(j_k^a + j_k^b \right) \tag{4}$$

where the volume diffusion fluxes refer to j_k^a etc. Two options are conceivable: balanced mass fluxes ($\sigma^a = -\sigma^b$) or balanced diffusion fluxes ($j_k^a = -j_k^b$). Since the interface is generally thin—particularly in the sharp interface limit, where both options are identical—the preference is related to the employed numerical method.

Most authors opt for a volume conservative approach, i.e., $j_k^a = -j_k^b$, and employ a volume averaged velocity field. In this case, mass is only globally conserved, provided that the inter facial regions do not intersect with the domain boundaries (Ding et al., 2007), which might be difficult for travelling waves. The continuity expression (4) conveniently simplifies to a zero velocity divergence, and the conservative momentum equations are augmented by a total mass flux term $v_i(\sigma^a + \sigma^b)$ on the r.h.s., cf. Eq. (6). On the contrary, assuming a mass conservative approach, i.e., $\sigma^a = -\sigma^b$, one has to account for divergence effects of the observed mass-averaged velocity.

2.1 Momentum and continuity

The present research opts for a mass-averaged velocity field v_i governed by the Navier-Stokes (NS) equations supplemented by a surface tension force f_i^{ST}:

$$\rho \frac{\partial v_i}{\partial t} + \rho v_j \frac{\partial v_i}{\partial x_j} = \frac{\partial}{\partial x_j}\left[2\mu_e S_{ij} - \left(p + \frac{2}{3}\mu_e \frac{\partial v_k}{\partial x_k} \right)\delta_{ij} \right] + \rho g_i + f_i^{\mathrm{ST}} \tag{5}$$

Assuming $\sigma^a = -\sigma^b$, the continuity equation follows from Eq. (2), and yields a conservative formulation for mass and momentum:

$$\frac{\partial \rho v_i}{\partial t} + \frac{\partial \rho v_j v_i}{\partial x_j} = \frac{\partial}{\partial x_j}\left[2\mu_e S_{ij} - \left(p + \frac{2}{3}\mu_e \frac{\partial v_k}{\partial x_k} \right)\delta_{ij} \right] + \rho g_i + f_i^{\mathrm{ST}} \tag{6}$$

$$\frac{\partial \rho}{\partial t} + \frac{\partial v_i \rho}{\partial x_i} = 0 \tag{7}$$

where ρ, μ_e, and p refer to the density, dynamic viscosity, and pressure of the mixture. The Kronecker delta and the strain-rate tensor are marked by δ_{ij} and $S_{ij} = \frac{1}{2}\left(\frac{\partial v_i}{\partial x_j} + \frac{\partial v_j}{\partial x_i} \right)$. The four right-hand side terms of the momentum balance Eq. (6) denote viscous, pressure, body, and surface tension forces. The pressure is a numerical property which often inherits further trace terms related to the adopted phase field model and surface tension force expression. The framework supports laminar and Reynolds-averaged (modelled) turbulent flows (RANS). In the latter case, v_i and p correspond to Reynolds-averaged properties and p is additionally augmented by a turbulent kinetic energy (k) term, i.e., $2\rho k / 3$. Along with the Bousinesq hypothesis, the dynamic viscosity $\mu_e = \mu + \mu_t$ of turbulent flows consists of a molecular and a turbulent contribution (μ_t), and the system is closed using a two-equation turbulence model to determine μ_t and k. Details of the turbulence modelling practice are omitted to save space and can be found in textbooks, e.g., Wilcox (1998).

2.2 Equation of state

We expect both fluid phases to be incompressible and virtually immiscible. Moreover, we assume no-slip between the fluid phases along the interface and model the flow as a mixture between fluids which share the velocity field governed by Eq. (6). The continuity equation (7) serves to determine the pressure and the local fluid properties ρ

and μ follow from an equation of state. A more general equation of state (EoS) refers to a weighted sum of the bulk properties of the participating phases, viz.,

$$\rho = m\rho_a + (1-m)\rho_b, \quad \mu = m\mu_a + (1-m)\mu_b \tag{8}$$

The normalized function $m(c)$ describes the transition of the properties and only depends on the concentration c. The volume concentration of the foreground phase is physically bounded by $c \in [0,1]$. A frequently employed simple choice for the transition function refers to a linear interpolation:

$$m = \begin{cases} 0, & c < 0 \\ c, & 0 \le c \le 1 \\ 1, & c > 1 \end{cases} \tag{9}$$

An alternative approach employed herein reads

$$m = \frac{1}{2}\left[\tanh\left(\frac{2c-1}{\gamma_m}\right)+1\right] \tag{10}$$

Here γ_m is a non-dimensional model parameter to adjust the transition regime. For $0.1 \le \gamma_m \le 0.5$ the difference between Eq. (9) and Eq. (10) is limited to 0.009%–3.597% at the transition points $c = 0$ and $c = 1$, resulting in a slight offset of fluid properties. The formulation (10) serves the regularization of unbounded concentration values and helps to sharpen partly blurred interfaces.

2.3 Diffusive interface model

The subsection briefly summarizes the diffusive interface model for isothermal two-phase flows as suggested in a landmark paper by Cahn and Hilliard (1958) and later elucidated by Jacqmin (1999). The present approach refers to a classical CH-model and is based upon the free energy E of the interface Γ between two isothermal fluid phases:

$$E = \int_\Gamma e \,\mathrm{d}\Gamma = \int_\Gamma \left(C_1 b(c) + \frac{C_2}{2}\left|\frac{\partial c}{\partial x_k}\right|^2 \right) \mathrm{d}\Gamma \tag{11}$$

The coefficients C_1 (Pa) and C_2 (N) can be determined from the interface thickness γ (m) and surface tension $\sigma_{a,b}$ (N/m) between the two fluids, as outlined below. The foreground phase concentration c represents a measure of phase and ranges from a foreground state (c_a) to a background state (c_b), i.e., $c_a = 1$ and $c_b = 0$. Mind that alternative CH-formulations exist, which employ the mass concentration or other energetic contributions.

The first term of e refers to the bulk energy density and aims to separate the fluids. The second term represents the gradient energy which widens the interface. To model separated (immiscible) fluids, a fourth-order polynomial, labeled "double well potential", is often used to describe the bulk energy density, i.e., $b(c) = (c-c_a)^2(c-c_b)^2$:

$$b(c) = (c-1)^2 c^2 \tag{12}$$

In equilibrium conditions, E is minimized with respect to c. Using variational calculus, this relates to the root of a chemical potential ψ for the equilibrium state of plane interfaces (i.e., $\psi = 0$):

$$\psi = \frac{\delta E}{\delta c} = C_1 \frac{\partial b}{\partial c} - C_2 \frac{\partial^2 c}{\partial x_n^2} \quad \rightarrow \quad C_1 \frac{\partial b}{\partial c} = C_2 \frac{\mathrm{d}^2 c}{\mathrm{d}x_n^2} \tag{13}$$

where x_n represents the interface normal direction. Substituting Eq. (12) into Eq. (13), one obtains a hyperbolic tangent concentration profile. This also renders a relation between the coefficients C_1, C_2 and an interface thickness γ, viz.,

$$c(x_n) = \frac{1}{2}\left(\tanh\left(\frac{2x_n}{\gamma}\right)+1\right) \quad \text{with} \quad \gamma := \sqrt{\frac{8C_2}{C_1}} \tag{14}$$

Similarly, surface tension forces can be related to the concentration. Jacqmin (1999) outlined that the convective rate of change of the free energy widens or compresses the interface. The term reads $\delta E/\delta c(v_i \partial c/\partial x_i) = \psi(v_i \partial c/\partial x_i)$ and should be balanced by the power $f_i^{\mathrm{ST}} v_i$ of the surface tension force f_i^{ST}. This immediately reveals the surface tension force used herein:

$$f_i^{\mathrm{ST}} = \psi \frac{\partial c}{\partial x_i} \tag{15}$$

Some authors rearrange this definition into an apparent pressure term and a term involving the chemical potential gradient (Song et al., 2019), i.e., $f_i^{\mathrm{ST}} = \partial(\psi c)/\partial x_i - c\,\partial\psi/\partial x_i$. Similarly, other authors employ the relation:

$$\psi \frac{\partial c}{\partial x_i} - \left[C_1 \frac{\partial b}{\partial x_i} + \frac{C_2}{2}\frac{\partial}{\partial x_i}\left(\frac{\partial c}{\partial x_k}\right)^2 \right] = -\frac{\partial}{\partial x_k}\left(C_2 \frac{\partial c}{\partial x_k}\frac{\partial c}{\partial x_i} \right) \tag{16}$$

to express the surface tension force by the divergence of a surface tension stress $-C_2(\nabla_k c)(\nabla_i c)$ and the gradient of a related apparent pressure $C_1 b + 0.5 C_2 (\nabla_k c)^2$ (Lowengrub and Truskinovsky, 1998; Abels et al., 2012). Expression (16) associates vanishing surface tension effects with $C_2 = 0$. Jacqmin (1999) also deduced a link between the surface tension and C_1, C_2 for a plane interface:

$$\sigma_{a,b} = C_2 \int_{-\infty}^{\infty} \left(\frac{\partial c}{\partial x_n}\right)^2 \mathrm{d}x_n \tag{17}$$

Substituting Eq. (14) into Eq. (17) yields

$$\sigma_{a,b} = \sqrt{\frac{C_1 C_2}{18}} \tag{18}$$

Once γ and $\sigma_{a,b}$ have been chosen, both CH coefficients can be determined from the plane interface relations (14, 18):

$$C_1 = 12\frac{\sigma_{a,b}}{\gamma}, \qquad C_2 = \frac{3}{2}\sigma_{a,b}\gamma \tag{19}$$

In the remainder of the paper, the neglect of the surface tension in under-resolved flows is modelled by $C_2 = 0$ N and, for the sake of simplicity, $C_1 = 1$ Pa . As will be shown in Section 5, this combination allows an estimation of the mobility parameter M, which in turn is introduced in the upcoming section.

2.3.1 *Concentration transport and velocity divergence*

The mixture fraction is computed from an additional transport equation that models the mass transfer between the phases. Two options will be discussed, referring to the classical VoF and the CH approach outlined in Section 2.3. Using the classical VoF approach, we assume that the material property of the fluid must not change, viz.,

$$\frac{\mathrm{d}c}{\mathrm{d}t} = \frac{\partial c}{\partial t} + v_i \frac{\partial c}{\partial x_i} = 0 \tag{20}$$

On the contrary, the CH-approach of Lowengrub and Truskinovsky (1998) refers to the mass concentration $c_m = c\rho_1 / \rho$ of the foreground phase and involves a diffusive phase transfer term:

$$\rho\frac{\mathrm{d}c_m}{\mathrm{d}t} = \frac{\partial}{\partial x_i}\left(M_m \frac{\partial \psi}{\partial x_i}\right) \tag{21}$$

Using the continuity relation (7) leads to

$$\frac{\partial \rho c_m}{\partial t} + \frac{\partial \rho v_i c_m}{\partial x_i} = \frac{\partial}{\partial x_i}\left(M_m \frac{\partial \psi}{\partial x_i}\right) \tag{22}$$

The desired conservative volume-flux based transport follows from Eq. (22), with $\rho c_m = \rho_1 c$ and $M_m = M / \rho_1$:

$$\frac{\partial c}{\partial t} + \frac{\partial v_i c}{\partial x_i} = \frac{\partial}{\partial x_i}\left(M \frac{\partial \psi}{\partial x_i}\right) \tag{23}$$

Here the mobility parameter M of dimension $\mathrm{m}^3 \cdot \mathrm{s/kg}$ ($\hat{=}\, v/\mathrm{Pa}$) is a free parameter that controls the strength of the phase separation process and will be explored for under-resolved flows in Section 5.

VoF methods for immiscible incompressible fluids are usually based upon a pressure correction/projection scheme and prefer to observe volume instead of the mass fluxes to avoid the density jump. The latter can be extended for hydrodynamic flows featuring $\partial v_i / \partial x_i = 0$ along the route outlined in Yakubov et al. (2015). Since the bulk densities are deemed incompressible, the density solely depends on the transition function m, which in turn depends on the concentration (9, 10). An alternative continuity equation is derived from Eq. (7):

$$\left(\frac{\rho_b - \rho_a}{\rho}\right)\frac{\partial m}{\partial c}\left(\frac{\partial c}{\partial t} + v_i \frac{\partial c}{\partial x_i}\right) = \frac{\partial v_i}{\partial x_i} \tag{24}$$

Substituting Eq. (23) into Eq. (24), one finally arrives at

$$\frac{\partial v_i}{\partial x_i} = f\frac{\partial}{\partial x_i}\left(M\frac{\partial \psi}{\partial x_i}\right)$$
$$\text{with} \quad f = \frac{f^*}{1 + f^* c} \quad \text{and} \quad f^* = \left(\frac{\rho_b - \rho_a}{\rho}\right)\frac{\partial m}{\partial c} \tag{25}$$

In conjunction with VoF, a solenoidal velocity field is recovered due to the neglect of diffusive mass transfer. Note that f^* is virtually zero in combination with the non-linear EoS (10) in the sharp interface limit, which returns a divergence-free velocity field.

2.4 Non-dimensional governing equations

The non-dimensional equations support the discussion of influences and assist the verification. Assuming a spatially constant mobility M, the non-conservative concentration, continuity and momentum equations read

$$\frac{1}{St}\frac{\partial c}{\partial t^*} + v_i^* \frac{\partial c}{\partial x_i^*} = \frac{1}{Pe}\frac{\partial^2}{\partial x_i^{*2}}\left(12\frac{\partial b^*}{\partial c} - \frac{3Ca^2}{2}\frac{\partial^2 c}{\partial x_k^{*2}}\right)\left(\frac{1}{1 + f^* c}\right)$$
$$= \frac{1}{Pe}\left(\frac{1}{1 + f^* c}\right)\frac{\partial^2 \psi^*}{\partial x_i^{*2}} \tag{26}$$

$$\frac{\partial v_i^*}{\partial x_i^*} = \frac{f}{Pe}\frac{\partial^2 \psi^*}{\partial x_i^{*2}} \tag{27}$$

$$\frac{\rho^*}{St}\frac{\partial v_i^*}{\partial t^*} + \rho^* v_j^* \frac{\partial v_i^*}{\partial x_j^*} + \frac{\partial}{\partial x_j^*}\left(Eup^*\delta_{ij} - \frac{2\mu^*}{Re}S_{ij}^*\right) - \frac{\rho^*}{Fn^2}g_i^*$$
$$= -\frac{2}{3}\frac{1}{Re}\frac{\partial}{\partial x_i^*}\left(\mu^*\frac{f}{Pe}\frac{\partial^2 \psi^*}{\partial x_i^{*2}}\right) + \frac{\psi^*}{We}\frac{\partial c}{\partial x_i^*} \tag{28}$$

The left-hand sides of the balance equations represent the classical, incompressible VoF-method. In the case of a non-zero right-hand side of Eq. (26), the velocity field is no longer divergence free in Eq. (27), which in turn introduces additional terms to the momentum balance (28). By way of example, the relationship between a dimensional quantity, a reference value, and a non-dimensional quantity marked with an asterisk reads $v_i = V v_i^*$. The dimensionless parameters are defined by

$$St = \frac{TV}{L}(\text{Strouhal}), \quad Eu = \frac{P}{\rho_b V^2}(\text{Euler})$$
$$Re = \frac{\rho_b VL}{\mu_b}(\text{Reynolds}), \quad We = \frac{\rho_b V^2 \gamma}{\sigma_{a,b}}(\text{Weber})$$
$$Fn = \frac{V}{\sqrt{GL}}(\text{Froude}), \quad Pe = \frac{VL\gamma}{M\sigma_{a,b}}(\text{Peclet})$$
$$Ca = \frac{\gamma}{L}(\text{Cahn}) \tag{29}$$

The quantities utilized for the non-dimensionalisation are given in Table 1. Local discrete similarity parameters employ $L = \delta x_i$, $T = \delta t$, and $V = \|v_i\|$, etc. It should be pointed out that the transition length γ can be small compared to a local grid spacing δx_i, resulting in small (discrete) Cahn-numbers, which supports the neglect of the second term on the r.h.s. of Eq. (26) in an under-resolved sharp interface limit.

Table 1 Quantities for the non-dimensionalisation of the governing equations

Field quantity	x_i	v_i	g_i	p	t	ρ	μ	c	ψ
Reference value	L	V	G	P	T	ρ_b	μ_b	1	$\sigma_{a,b}/\gamma$

3 Numerical procedure

Results of the present study are obtained from the Navier-Stokes procedure FreSCo$^+$ (Rung et al., 2009). The implicit finite volume procedure uses a segregated algorithm based on the strong conservation form and employs a cell-centred, co-located storage arrangement for all transport properties. Unstructured grids, based on arbitrary polyhedral cells or hanging nodes, can be used. The solution is iterated to convergence using a modified pressure-correction scheme (Yakubov et al., 2015). Various turbulence-closure models are available with respect to statistical (RANS) or scale-resolving (LES, DES) approaches. Time derivatives are approximated by an implicit Euler or implicit three time level (ITTL) scheme. The numerical integration employs a second-order mid-point rule, diffusive fluxes are determined from second-order accurate central differencing, and convective fluxes use higher-order upwind biased interpolation formulae. Since the data structure is generally unstructured, suitable preconditioned iterative sparse-matrix solvers for symmetric and non-symmetric systems, e.g., GMRES, BiCG, QMR, CGS, or BiCGStab, are used. The procedure is parallelized for several thousand processes using a domain decomposition method and the MPI communications protocol (Yakubov et al., 2013). It supports local mesh refinement, overset grids (Völkner et al., 2017), node-based adjoint shape-optimization (Kröger and Rung, 2015; Kröger et al., 2018), and fluid-structure interactions between mechanically coupled floating bodies (Luo-Theilen and Rung, 2017).

Cell-centred fluid properties are determined from Eq. (8). For face-based properties, a linear interpolation between adjacent cell-centre values is used. The discretization of the additional terms that originate from the CH-NS approach are discussed in the upcoming lines for equations (23 - concentration), (25 - continuity), and (6 - momentum). The discussion refers to the symbolic finite-volume approximation of a variable ϕ located in the center P of a control volume of size $\delta\Omega_P$, with neighbour control columns NB, i.e., $A_P\phi_P - \sum_{NB} A_{NB}\phi_{NB} = S_\phi \delta\Omega_P$. Here, the right-hand side source term S_ϕ is treated explicitly during the (time-implicit) iteration of a segregated solution procedure (Ferziger and Perić, 2012). All presented own VoF studies employ the compressive HRIC scheme for convective concentration transport (Muzaferija and Peric, 1999).

3.1 Concentration conservation

The numerical solution of Eq. (23) follows a deferred correction approach. Hereto the right-hand side is notionally split into a bulk density contribution and a gradient term, i.e., $\nabla_i[M(\nabla_i\psi)] = \nabla_i[M(\nabla_i(C_1\partial b/\partial c)] + \nabla_i[...]$. Using $\nabla_i b = (\partial b/\partial c)\nabla_i c$ and $\partial^2 b/\partial c^2 = 2 + 12c(c-1)$, an inherently positive contribution to the bulk density term is identified. This leads to an implicit contribution and an explicit source S_c which uses values of the previous iteration:

$$\frac{\partial}{\partial x_i}\left(M\frac{\partial\psi}{\partial x_i}\right) = \frac{\partial}{\partial x_i}\left(2MC_1\frac{\partial c}{\partial x_i}\right) + \underbrace{\left[\frac{\partial}{\partial x_i}\left(M\frac{\partial\psi}{\partial x_i}\right) - \frac{\partial}{\partial x_i}\left(2MC_1\frac{\partial c}{\partial x_i}\right)\right]}_{S_c} \tag{30}$$

The integration over a control volume yields a discretized surface integral over all sub surfaces, i.e., $\delta\Gamma_i^{(f)}$ of $\delta\Omega_P$ for the implicit part of Eq. (30) $\sum_{f(\delta\Omega_P)}(2MC_1)\nabla_i c\,\delta\Gamma_i$, which is discretized using central differences and the mid-point integration rule. The explicit source term follows from a mid-point integration over the control volume. Upwind biased schemes are used to approximate the convective fluxes of Eq. (23) for the CH approach and a compressive downwind biased approach (Muzaferija and Peric, 1999) is used for the VoF approach.

3.2 Momentum and mass conservation

A simple mid point integration is employed to account

for the additional explicit CH-NS sources. This involves $f\nabla_i(M\nabla_i\psi)\delta\Omega_P$ for the conservation of mass (25) in combination with a pressure correction scheme (Yakubov et al., 2015), and $f_i^{ST}\delta\Omega_P$ (15) for the momentum equation (6).

4 Verfication

4.1 Planar Couette flow

The implementation is verified for a planar Couette flow under the influence of vertical gravity, wherefore a non-dimensional analytical solution is constructed and compared with the numerical results. Figure 1 illustrates the considered test case and the employed numerical grid which involves 50×600 control volumes. The channel height refers to h. The lower half of the channel is filled with a dense background fluid and the free surface follows along a horizontal line $x_2 = h/2$, where the origin of the coordinate system is located at the bottom wall. The bottom wall is at rest and the top wall moves with $v_1 = v_{top}$ along the horizontal direction. Field values are non-dimensionalised with the reference quantities, $V = v_{top}$, $L = h$, and $P = \rho_b \,||\, g_i \,||\, h$ as well as the non-dimensional equation system (26–28) is used.

The velocity is assumed to be unidirectional, i.e., $v_1^*(x_2^*)$, and in a fully developed, laminar, steady state. Moreover, the concentration field is also considered steady and homogeneous in the primary direction (x_1^*), viz.,

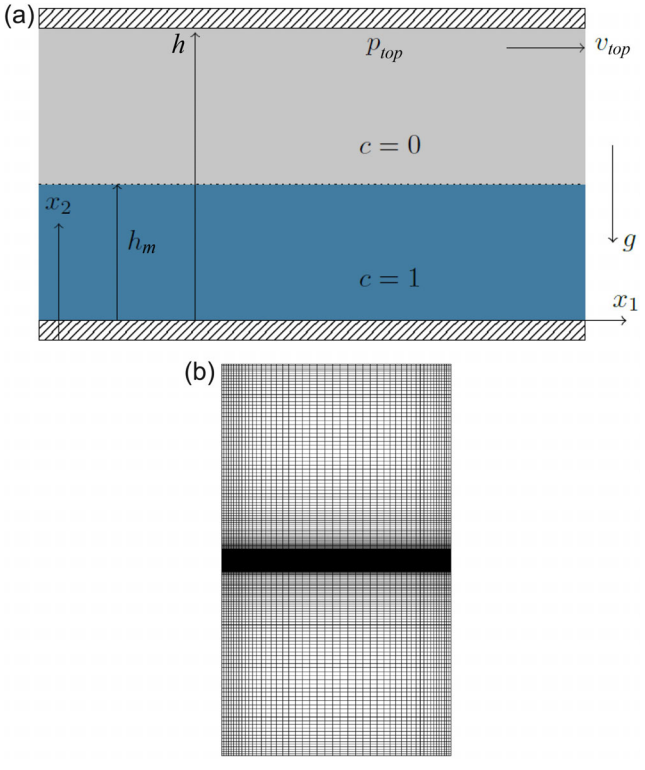

Fig. 1 (a) Setup of the planar Couette flow verification case and (b) employed computational grid.

$$C: \quad \frac{\partial^2}{\partial {x_2^*}^2}\left(4c^3 - 6c^2 + 2c - Ca^2\frac{\partial^2 c}{\partial {x_2^*}^2}\right) = 0 \tag{31}$$

$$R_1: \quad \frac{\partial}{\partial x_2^*}\left(\mu^*\frac{\partial v_1^*}{\partial x_2^*}\right) = 0 \tag{32}$$

$$R_2: \quad Eu\frac{\partial p^*}{\partial x_2^*} - \frac{1}{Fn^2}\rho^* g_2^* = 0 \tag{33}$$

Using the linear EoS (9) allows an integration of Eqs. (31)–(33) and results in the following analytical solution:

$$c = \frac{1}{2}\left(\tanh\left(Ca^{-1}\left(2x_2^* - 1\right)\right) + 1\right) \tag{34}$$

$$v_1^* = \frac{4x_2^* + Ca\left(\mu_a^* - 1\right)\log\left(\frac{\mu_a^* + 1 + \left(1-\mu_a^*\right)\tanh\left(Ca^{-1}\right)}{\mu_a^* + 1 - \left(1-\mu_a^*\right)\tanh\left(Ca^{-1}\left(2x_2^* - 1\right)\right)}\frac{\tanh\left(Ca^{-1}\left(2x_2^* - 1\right)\right) + 1}{1 - \tanh\left(Ca^{-1}\right)}\right)}{4 + Ca\left(\mu_a^* - 1\right)\log\left(\frac{\mu_a^* + 1 + \left(1-\mu_a^*\right)\tanh\left(Ca^{-1}\right)}{\mu_a^* + 1 - \left(1-\mu_a^*\right)\tanh\left(Ca^{-1}\right)}\frac{\tanh\left(Ca^{-1}\right) + 1}{1 - \tanh\left(Ca^{-1}\right)}\right)} \tag{35}$$

$$p^* = \frac{1}{EuFn^2}\left[\rho_a^*\left(1 - x_2^*\right) + \frac{Ca\,\rho_\Delta^*}{4}\log\left(\frac{\tanh\left(Ca^{-1}\left(x_2^* - 1\right)\right) + 1}{\tanh\left(Ca^{-1}\right) + 1}\right)\right] \tag{36}$$

This solution follows from Dirichlet conditions for the concentration and velocities along the top as well as the bottom wall ($v_1^*(1) = c(0) = 1, v_1^*(0) = c(1) = 0$). Additionally, a prescribed top-wall pressure ($p^*(1) = 0$) is employed. Interestingly, the solution is independent from the Peclet number and thus also from the mobility parameter M.

Computational results for the CH-NS system (6, 23, 25) are obtained on a 2D grid in conjunction with periodic boundary conditions in stream wise direction. Convective fluxes for momentum and concentration are discretized using first-order upwind differencing (UDS) and the mobility is assigned to a value that results in $Pe = 1\times10^5$. Predictive results are compared with analytical solutions for a range of Cahn numbers ($Ca_h = 0.2, 0.1, 0.02$), viscosity ratios ($\mu_a^* = 0.25, 1, 4$) and density ratios ($\rho_a^* = 0.25, 1, 4$) along with exemplary flow conditions of $Re = 100$, $Fn = 0.5$, and $Eu = 4$. The vertical interface resolution involves 20, 100, or 200 control volumes depending on the Cahn number.

Numerical results extracted along the centre vertical line are displayed in Fig. 2. The left graph compares analytical and computed concentration profiles for three different Cahn numbers. A comparison of results obtained for different fluid properties at $Ca_h = 0.1$ is displayed in the other two graphs of the figure. All comparisons reveal an excellent predictive agreement with the analytical solutions (34–36).

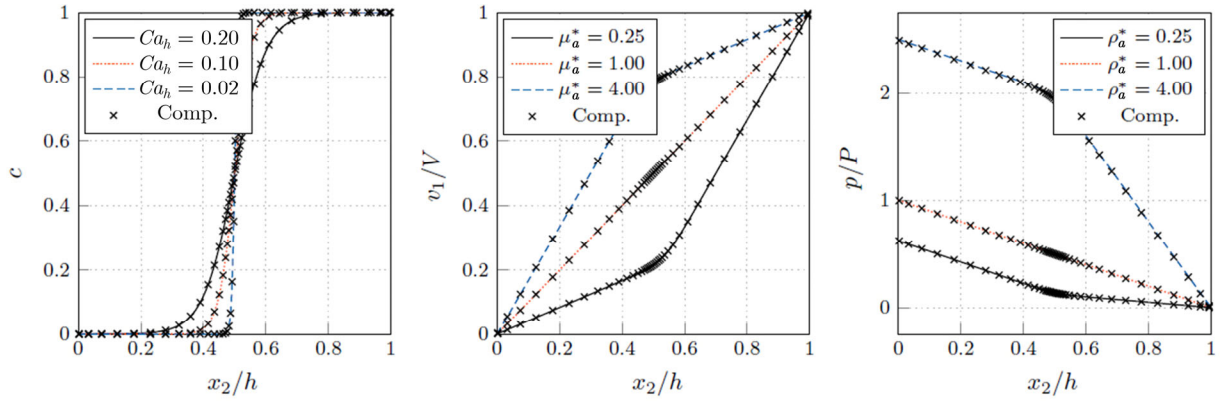

Fig. 2 Comparison of numerical and analytical results for the planar Couette flow example at $Re = 100$, $Fn = 0.5$, $Eu = 4$, and $Pe = 1\times10^5$. Left: Concentration profiles for different Cahn numbers. Middle: Velocity profiles for different viscosity ratios ($Ca_h = 0.1$). Right: Pressure profiles for different density ratios ($Ca_h = 0.1$).

4.2 Stationary bubble

The influence of the surface tension model is verified by computing the transition from an initial non-equilibrium (rectangular) bubble into an equilibrium (circular) bubble. The example is restricted to advancing a 2D flow field without gravitational effects ($Fn = \infty$) in pseudo time. As outlined in Fig. 3, a lighter foreground phase (ρ_a / ρ_b =1/100) rectangle with an edge length of $L = 0.005$ m is initially embedded into a heavier phase, such that the surface tension directs the shape of the interface towards a circle. Equal viscosities are employed for both fluids. Due to the symmetrical arrangement, only one quarter of the bubble is simulated on a homogeneous isotropic grid. Symmetry conditions are placed along the two main axes and the outer boundaries of the domain. The grid employs 550×550 control volumes to cover the quartered domain of $L\times L$. The Cahn number based on the initial edge length L reads $Ca_L = 0.02$ and the transition is resolved by 11 control volumes. In line with an assumed unit Reynolds number, we define the reference velocity as $V = \mu_b / (\rho_b L)$. The mobility and the surface tension are chosen to end up with Peclet and Weber numbers $Pe_L = 4\times10^4$ and $We = 800$ respectively.

As observed in Fig. 3(a), the rectangular bubble deforms into a circle over time. In addition the figure indicates the temporary velocity vectors which decay in time. In the final state, the pressure difference between the bubble centre and a far outside location reads $\Delta p = 2.0$ Pa, which matches the result of the 2D Young-Laplace law, i.e., $\Delta p = \sigma_{a,b} / R$, and also indicates the correct prediction of the final bubble radius $R = L / \sqrt{\pi}$. To underline the correct pressure approximation, the same situation is simulated with an increased transition length for three different surface tension values $\sigma_{a,b} = 0.5, 0.25, 0.0625$ (N/m) at $Ca_L = 0.1$, $Pe_L = 200$ (N/m)$/\sigma_{a,b}$, $We = 4$ (N/m)$/\sigma_{a,b}$. Figure 3(b) shows

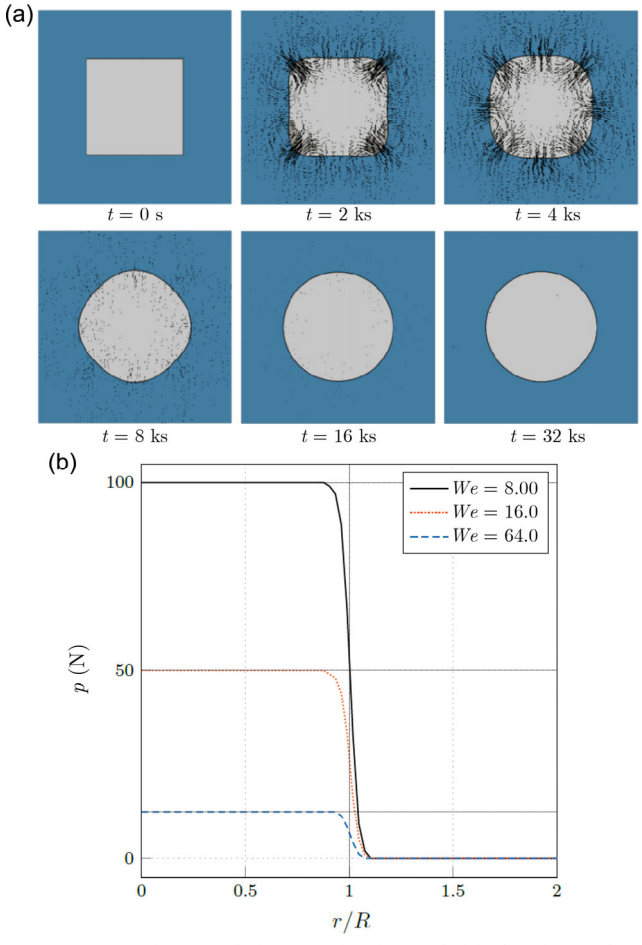

Fig. 3 (a) Evolution of shape and velocity fields for the surface tension driven transition from an initially rectangular to a round bubble (ks refers to 10^3 seconds) and (b) computed pressure distribution along a radial slice that originates in the center of a bubble with radius $R = L / \sqrt{\pi}$ for different surface tension coefficients $\sigma_{a,b} = 0.5, 0.25, 0.0625$ (N/m) at $Ca_L = 0.1$, $Pe_L = 200$ (N/m)$/\sigma_{a,b}$, and $We = 4$ (N/m)$/\sigma_{a,b}$. Grey horizontal lines in (b) indicate the expected interior pressure obtained by the Young-Laplace law.

the resulting pressure distributions over a radial coordinate which reveal a fair agreement with theoretical results.

5 Mobility parameter in under-resolved flows

The section discusses means to model the mobility parameter in under-resolved flow simulations, where the surface tension influence is neglected due to the coarse resolution of the interface thickness γ. As outlined in Section 2.3, the neglect of surface tension yields $C_2 = 0$ and the concentration equation (25) simplifies towards

$$\frac{\partial c}{\partial t} + \frac{\partial v_i c}{\partial x_i} = \frac{\partial}{\partial x_i}\left(M \frac{\partial}{\partial x_i}\left(C_1 \frac{\partial b}{\partial c} \right) \right) \tag{37}$$

Using $\nabla_i b = (\nabla_i c)\partial b / \partial c$ together with the definition of the double well potential b (12), the r.h.s. of Eq. (37) reads

$$\begin{aligned} \frac{\partial}{\partial x_i}\left(M \frac{\partial}{\partial x_i}\left(C_1 \frac{\partial b}{\partial c} \right) \right) &= \frac{\partial}{\partial x_k}\left[M C_1 \left(12c^2 - 12c + 2 \right) \frac{\partial c}{\partial x_k} \right] \\ &= \frac{\partial}{\partial x_k}\left(v_c \frac{\partial c}{\partial x_k} \right) \end{aligned} \tag{38}$$

Depending on the concentration value, Eq. (38) acts locally diffusive ($v_c \geq 0$) or compressive ($v_c < 0$). The sign-change of the apparent viscosity $v_c = 2C_1 M(6c^2 - 6c + 1)$ resembles compressive approximations of the convective term, which switch from upwind to downwind approximations along the interface, and thus from positive to negative (apparent) viscosities, to keep the interface sharp (Muzaferija and Peric, 1999; Ubbink and Issa, 1999). The apparent viscosity in Eq. (38) zeroes at $c = 0.5(1 \pm 1/\sqrt{3})$ and is negative over approximately 58% of the transition region. Aiming at a closure for the mobility parameter in under-resolved simulations, we separate the mobility into a physical and a modelled part, i.e., $M = M^{\text{phys}} + M^{\text{mod}}$. The physical part is usually assigned to fairly small values, e.g., $M^{\text{phys}} \ll 1 \times 10^{-15}$ m$^3 \cdot$s/kg (Jacqmin, 2000; Magaletti et al., 2013). Jacqmin (1999) reported that the mobility typically scales with the transition length $M \propto \gamma^n$, where n varies between $1 \leq n \leq 2$. Moreover, a recent publication of Magaletti et al. (2013) suggests $n = 2$ and thus $Pe \approx Ca^{-1}$ or $\gamma \approx \sqrt{\sigma_{a,b} M / V}$. Most engineering settings are therefore unable to sufficiently resolve the transition length and we consider the numerical contribution M^{mod} to be dominant.

5.1 Homogeneous mobility model

The formulation of M^{mod} is based on the interface blurring introduced by upwind-biased schemes. An estimation of the tensorial numerical diffusion at a cell face returned by a first-order upwind scheme might read

$$v_{ij}^{\text{UDS}\,(f)} = (\lambda \delta x_j v_i)^{(f)} \tag{39}$$

Here $v_i^{(f)}$ denotes the velocity at the face center, $\delta x_j^{(f)}$ refers to the connecting vector from the upstream to the downstream adjacent cell center, and $\lambda \delta x_j^{(f)}$ approximates the distance between the face and the upstream cell. Depending on the time discretization scheme, the related error might be included into the estimate of the mobility parameter from a modified equation analysis. For the example of a first-order implicit time discretization, the modified equation analysis suggests a simple supplement of a Courant number term, i.e., $v_{ij}^{\text{UDS}\,(f)}{}_{\text{unsteady}} = v_{ij}^{\text{UDS}\,(f)} \left(1 + Co_{i,j}^{(f)} \right)$. The estimate (39) is spatially and temporally variable. Spatially volatile mobility distributions are deemed to obstruct the robustness of the procedure. Hence, we confine our interest to homogenized approaches and estimate the mobility based on the maximum norm of the matrix valued numerical diffusion:

$$\begin{aligned} M^{\text{mod}} = & \frac{\tilde{M}}{C_1 \left| \left\{ n_f : \delta x_i \frac{\partial c}{\partial x_i}^{(f)} \geq \delta_c \right\} \right|} \cdot \\ & \sum_f^{n_f} \begin{cases} \max_{i,j} \left(| \lambda \delta x_j v_i | \right)^{(f)}, & \delta x_i \frac{\partial c}{\partial x_i}^{(f)} \geq \delta_c \\ 0, & \text{otherwise} \end{cases} \end{aligned} \tag{40}$$

Note that the field is filtered to extract the interface region, i.e., only faces with a projected concentration gradient above $\delta_c = 10^{-3}$ are considered. A von-Neumann stability analysis of the first-order discretized 1D equation at the interface location ($c = 0.5$) yields the following estimates for stable solutions (cf. Appendix):

$$\tilde{M} \leq 1 \qquad \text{and} \qquad \tilde{M} \geq \left[1 + \frac{2}{Co(1 - \cos\varphi)} \right] \tag{41}$$

where φ represents the phase angle. Approaching the steady state limit, the analysis only excludes $\tilde{M} = 1$. In the case of $\varphi \to 0$, the branch $\tilde{M} \leq 1$ might be a safer recommendation. Therefore $\tilde{M} = 0.1$ is used for all applications displayed in Section 6, for which no stability problems are observed. If alternative convection schemes are used, the 1st-order upwind based analysis still provides reliable estimates.

Further inspection reveals that under no circumstances the predicted phase transition spans less than five control volumes. Improved sharpening is obtained from the non-linear equation of state (10). An illustrative 1D example is used to demonstrate this. In this example, a free surface is transported by a prescribed flow field on the grid depicted in Fig. 4(a). The horizontal flow field is directed from left to right with a constant velocity of $v_1 = 1$ m/s, and only the concentration equation (23) is computed. The employed

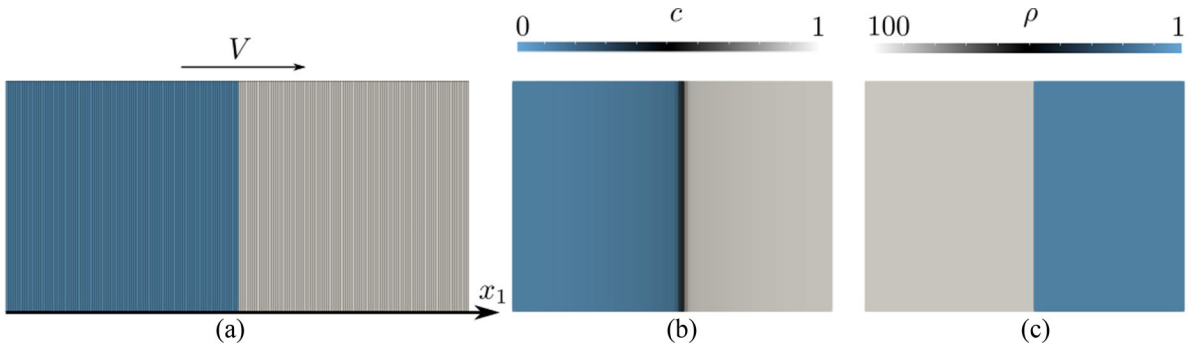

Fig. 4 (a) Computational grid with initial conditions for a 1D concentration advection, (b) slightly blurred interface predicted by a CH-NS simulation using $\tilde{M} = 0.1$ and $Co = 1$ after $t = 5$ s, and (c) corresponding density field returned by the non-linear equation of state (10; $\gamma_m = 0.05$).

grid is homogeneous ($\lambda = 0.5$) and features $\delta x_1 = 10^{-3}$ m and $\delta x_2 = 1$ m. The simulation is initialized with a sharp interface along a vertical line at the centre location $x_1 = 1$ m. Figure 4(b) displays a partly blurred interface from one CH simulation with $\tilde{M} = 0.1$ and $Co = 1$ after $t = 5$ s. The corresponding density field obtained from the non-linear equation of state using $\gamma_m = 0.05$ is displayed in Fig. 4(c). Although the concentration field is slightly blurred, the resulting density and viscosity fields are sharp.

A second 2D example refers to a circle of radius $r / L = 0.15$ that is initially placed at $x_i / L = [0.5, 0.75]^{\mathrm{T}}$ in a square of unit length ($L = 1$ m) as described in Rider and Kothe (1998). In this frequently employed validation example, the free surface is advected under a spatial deforming velocity field $v_1 = -\partial\Theta / \partial x_2$, $v_2 = \partial\Theta / \partial x_1$ where $\Theta = \sin^2(x_1\pi)\sin^2(x_2\pi) / \pi$ defines the stream function. Above all, we would like to show that the proposed approach allows for courant numbers $O(1)$ and has resharpening capabilities also under complex and large interface deformations. Therefore, a comparatively fine numerical grid with $\delta x_i / L = 1 / 400$ is used combined with $\delta t = Co\,\delta x_i / V$ and $Co = 2$ as well as $V = 1$ m/s in accordance to the maximum value from the stream function definition. Symmetry boundary conditions are used and second order approximations are conducted for transient (ITTL), convective (QUICK), and diffusive (CD) terms. Results are assessed by means of the predicted interface sharpness and the spatial progression of the interface over time. A local sharpness indicator quantity q is used to judge the interface quality. The latter employs the computed concentration gradient at an interfacial face and multiplies this with twice the grid-spacing, i.e., $q^{-1} = 2\delta x_i (\partial c / \partial x_i)_{(c=0.5)}$. In the present example, an interfacial face is a face that is adjacent by one cell featuring $c < 0.5$ and one cell featuring $c > 0.5$. A perfectly sharp interface results in $q = 1$, acceptable interfaces follow from $q < 3$ and a global reference is determined by the arithmetic average of all local sharpness indicators q, labeled Q.

Three CH-NS simulations are performed. Two simulations refer to temporally constant mobility parameter values $\tilde{M} = 1$ and $\tilde{M} = 0.01$, which should feature measurable differences on the predicted sharpness. In the third case, $\tilde{M}$ switches between the two constant values, i.e., $\tilde{M}(1\text{ s} \le t \le 2\text{ s}) = 0.01$ and $\tilde{M}(t < 1\text{ s}, 2\text{ s} < t) = 1$. The evolution of the advected concentration over time is displayed in Fig. 5(a) for the switching mobility parameter case. In the first and last third of the simulation the interface remains practically sharp, which is no longer the case for the time $1\text{ s} \le t \le 2\text{ s}$ where the lower choice of $\tilde{M}$ is not able to overcome the numerical diffusion. The visible temporary blurring is also displayed by the sharpness indicator in Fig. 5(b) (bottom) that underlines the (on-the-fly) resharpening capability and the competent predictive performance of the CH-NS in comparison to VoF schemes (HRIC; $Co = 0.2$).

6 Validations and applications

6.1 Gravity and capillary wave

The first example deals with the decay of standing waves which are initialized according to Fig. 6(a). We aim to assess, if the shear driven energy exchange between the two fluids, labelled *a* and *b*, is correctly captured in both, the capillary and the gravity regime under the influence of vertical gravitational acceleration g_2. Numerical results are compared with analytical solutions of Prosperetti (1981), which exist for identical kinematic viscosities ($\mu_a / \rho_a = \mu_b / \rho_b$) in the linear (laminar) flow regime. The initial wave length complies with a unit wave number ($k = 2\pi / \lambda = 1$) and the initial wave amplitude corresponds to $a = 0.01\lambda$. The reference velocities refer to $V = \sqrt{|g_2|\lambda}$ and $V = \sqrt{\sigma_{a,b} / (\lambda\rho_b)}$ for the gravity and the capillary case, respectively. The extent of the 2D computational domain depicted in Fig. 6(b) reads $\lambda \times \lambda$. A locally refined grid with approximately 250.000 isotropic control volumes is employed. The resolution of the free surface region refers to $\delta x_1 = \delta x_2 = \lambda / 4000$. The

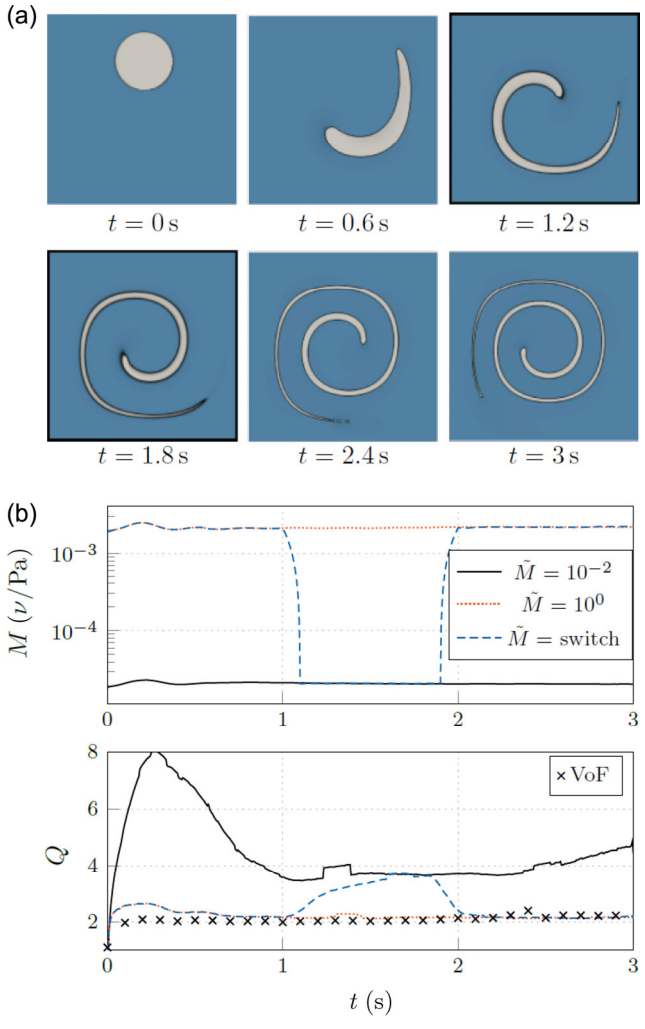

Fig. 5 Time evolution of (a) the concentration contour for a prescribed mobility of $\tilde{M} = 1$ that is reduced to $\tilde{M} = 0.01$ between $1\,\mathrm{s} \le t \le 2\,\mathrm{s}$ and (b) mobility M (top) and global sharpness indicator Q (bottom) over the simulation time for different under-resolved CH-NS simulations at $Co = 2$.

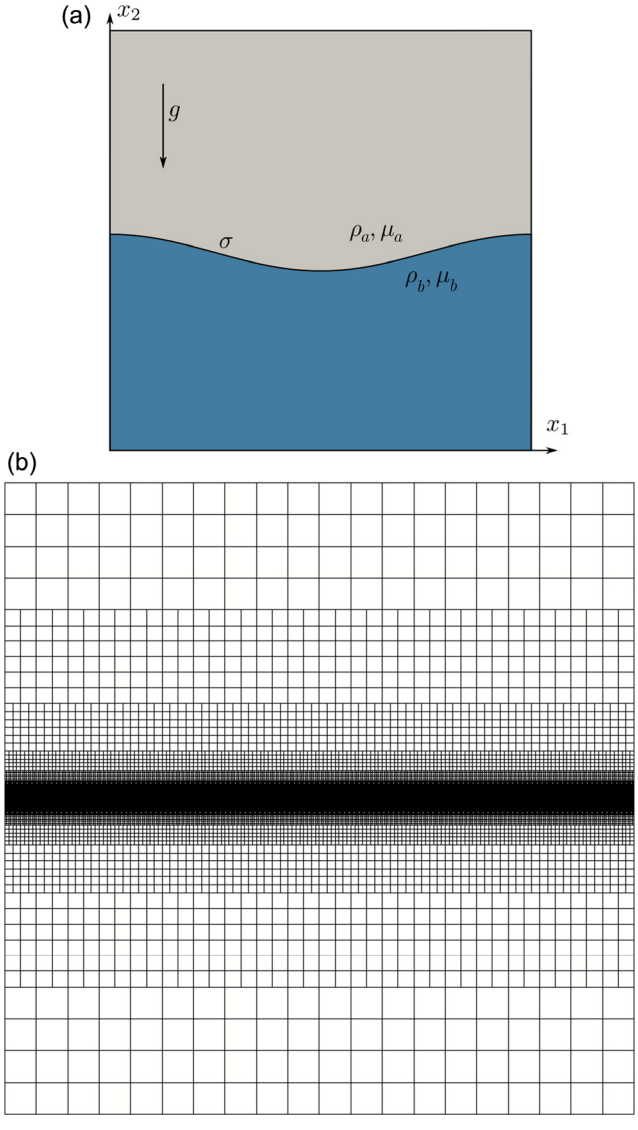

Fig. 6 (a) Initial setup of the standing wave case (scaled for visualization purposes) and (b) employed computational grid.

time step is assigned to $\delta t = \lambda / (4000V)$ which is sufficient to ensure Courant numbers below $Co < 0.1$. Symmetry (no-slip) conditions are used along constant x_1 (x_2) boundaries of the domain.

For the gravity wave, surface tension influences are neglected and the density ratio and Reynolds-number read $\rho_a / \rho_b = 1/100$ and $Re = V\lambda / \nu_b = 1000$. The CH-NS simulations are based on the mobility estimation described in Section 5 and the non-linear material law ($\tilde{M} = 0.1$, $\gamma_m = 0.1$). Figure 7(top) displays the evolution of the free-surface elevation at the horizontal left end ($x_1 = 0$) predicted by CH-NS and VoF next to the analytical solution of Prosperetti. In comparison to the linear theory, the top figure reveals a slightly stronger wave damping and a minor phase shift returned by the CH-NS approach for the gravity case, which outperforms the present VoF method. The latter is a consequence of the resharpening character of the CH-NS approach.

For the capillary case, the density and viscosity ratios read $\rho_a / \rho_b = 1/100$ and $\mu_a / \mu_b = 1/10$ respectively, the interface thickness is resolved by 10 vertical cells and follows from a Cahn number of $Ca_\lambda = \gamma / \lambda = 1/400$. The Ohnesorge number adjusts the surface tension force σ and reads $Oh = \mu_b / \sqrt{(\sigma_{a,b} \lambda \rho_b)} = 1/100$. The mobility parameter is prescribed in accordance with a Peclet number of $Pe_\lambda = 2 \times 10^{10}$ together with the linear materiallaw. Conclusions drawn for the capillary case are similar to the gravity case, as indicated by Fig. 7(bottom), which compares the evolution of the wave amplitude at the horizontal left end ($x_1 / \lambda = 0$) predicted by the present CH-NS with the analytical solution of Prosperetti.

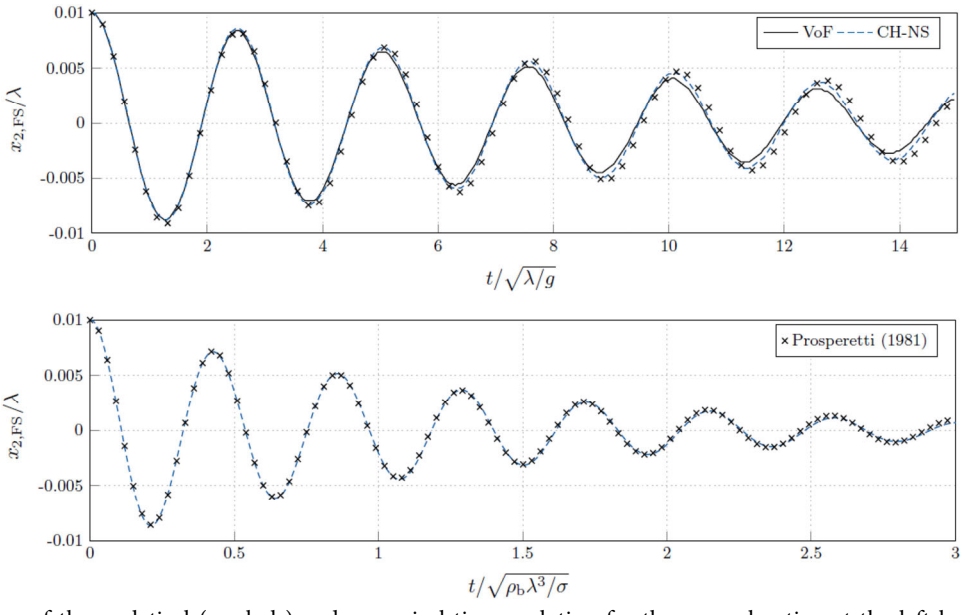

Fig. 7 Comparison of the analytical (symbols) and numerical time evolution for the wave elevation at the left boundary ($x_1 = 0$) obtained for the gravity (top) and the capillary (bottom) case.

6.2 Submerged hydrofoil

The second example refers to the wave pattern downstream of a submerged NACA0012 hydrofoil at 5° incidence in accord with experimental data of Duncan (1981, 1983), cf. Fig. 8(a). The chord length to submergence ratio at the leading edge of the foil reads $c / L = 7 / 9$. The study is performed for a turbulent flow at $Re = v_1 c / v_b = 144855$ and $Fn = v_1 / \sqrt{GL} = 0.567$, based on the gravitational acceleration G, the inflow velocity v_1, and the kinematic viscosity of the water v_b. The two-dimensional domain has a length and height of $75c$ and $25c$, where the inlet and bottom boundaries are located 10 chord-lengths away from the origin. A dimensionless wave length of $\lambda^* = \lambda / L = 2\pi Fn^2 = 2.0193$ is expected.

The utilized unstructured numerical grid is displayed in Fig. 8(b) and consists of approximately 150,000 control volumes. The fully turbulent simulations employ a wall-function based $k-\omega$ SST model (Menter et al., 2003) and all convective terms are approximated using the QUICK scheme. At the inlet, velocity and concentration values are prescribed, slip walls are used along the top and bottom boundaries, and a hydrostatic pressure boundary is employed along the outlet. The wall normal distance of the first grid layer reads $y^+ \approx 30.0$ and the free surface refinement employs approximately $\delta x_1 / \lambda = 1/100$ cells in the longitudinal as well as $\delta x_2 / \lambda = 1/400$ cells in the normal direction. The VoF approach is integrated in pseudo time with a time step size of $\delta t = (\delta x_2 / V) Co$ together with $Co = 0.1$. The CH-NS results are obtained from a steady state approach.

The study neglects surface tension due to an under-

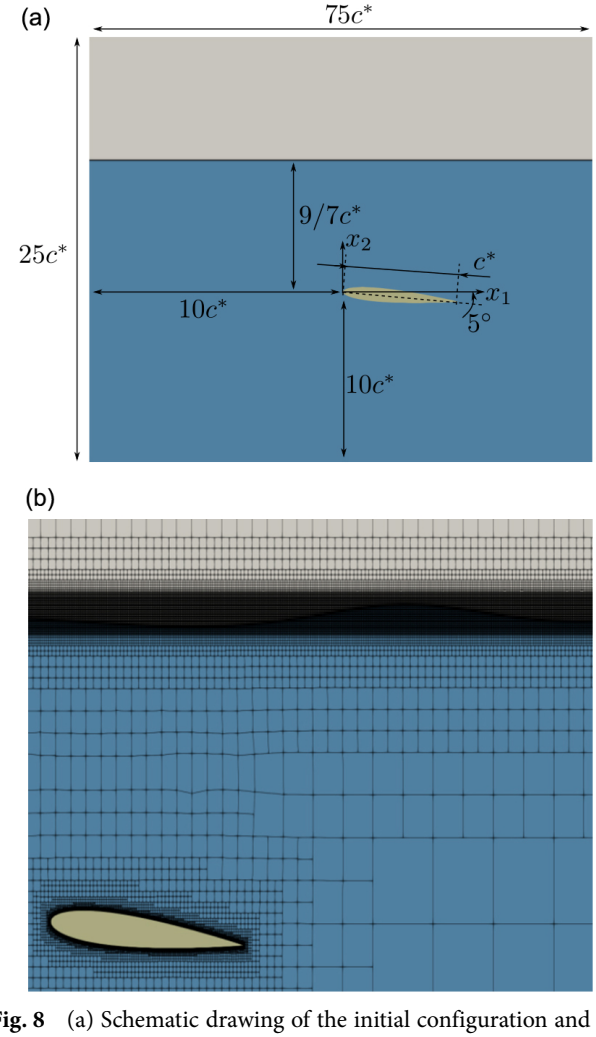

Fig. 8 (a) Schematic drawing of the initial configuration and (b) unstructured numerical grid around the foil and the free surface.

resolved interface thickness and employs both the linear (9) as well as the non-linear EoS (10; $\gamma_m = 0.1$). The surface tension force is neglected in the momentum equation and the concentration equation utilizes $C_2 = 0$ N and $C_1 = 1$ Pa. Figure 9(a) shows the wave elevation for two CH-NS simulations with the same modelled mobility parameter ($\tilde{M} = 0.1$) but different EoS next to the result of a VoF simulation. The non-linear EoS outperforms the linear version and drives the CH-NS approach closer to the experimental data as well as to the VoF result. Similar to the results displayed in Fig. 4, the linear model provides slightly blurred density fields which translates into a reduction of the wave amplitude. Figure 9(b) tracks the drag force coefficient over the simulation time t_{sim} for the VoF and the non-linear CH-NS simulations. The predicted drag differs about 0.4% and a speed up of approximately one order of magnitude is achieved through the Courant-number independent CH-NS approach. Detailed qualitative and quantitative CPU-efforts are given in Table 2.

6.3 Flow around a KCS container vessel

The final application refers to the fully turbulent flow around an unappended Kriso container ship hull (KCS). Experimental resistance data and wave fields are published by Kim et al. (2001) for a 1:31.6 scale model and a large amount of comparative numerical data exists, e.g., Banks et al. (2010), Larsson et al. (2010), Manzke et al. (2013), Kröger (2016), and Kröger et al. (2018). The distance between aft and front perpendiculars of the hull model serves as a reference length $L = 7.2786$ m ($= L_{pp}$). Other reference values refer to the gravity acceleration G, the inflow velocity magnitude V, and the kinematic viscosity of the water ν_b. The model scale investigations refer to Reynolds- and Froude-numbers of $Re = VL/\nu_b = 1.4\times10^7$ and $Fn = V/\sqrt{GL} = 0.26$. The hull is fixed at the full scale static draught with zero trim and the motion and propulsion of the ship are suppressed during the simulation and the experiments.

The numerical grid consists of approximately 14.6 million unstructured hexahedral cells. The domains extend over $5L$, $1.75L$, $2.5L$ in longitudinal (x_1), lateral (x_2), and vertical (x_3) direction. Due to symmetry only half of the flow field is simulated. The inlet is located upstream at $x_1 / L_{pp} = 3$ and the free surface is initialized at $x_3 / L_{pp} = 1.75$ over the lower boundary of the domain. The surface of the hull is discretized with approximately 300,000 surface elements. The wall normal resolution of the hull refers to a dimensionless wall distances of $30 \leq y^+ \leq 100$ and justifies the use of wall functions. The vertical resolution of the free surface region is constant throughout the domain and attempts to resolve the expected wave amplitude of $5\times10^{-4} L_{pp}$ by hundred cells in the immediate vicinity of the hull. The tangential resolution of the free surface is refined within a Kelvin-Wedge to capture the resulting wave pattern. Based on the current Froude-number a dimensionless wavelength of $\lambda / L_{pp} = 2\pi Fn^2 = 0.4247$ is expected, which is approximated with roughly 100 cells. Figure 10 indicates the different refinement levels for the near and the far field.

At the inlet, outlet, outer, and lower boundaries, Dirichlet values for velocity and concentration are specified, while the pressure is extrapolated. A reverse situation is given at the top face which corresponds to a pressure boundary. Symmetry and wall boundary conditions are declared along the midship plane as well as the hull. Turbulence is modelled by a high-Re $k-\varepsilon$ model (Wilcox, 1998). Convective momentum transport is realized by a monotonicity-preserving QUICK scheme. Similar to the hydrofoil case, data obtained from CH-NS simulation is compared with VoF results. CH-NS calculations refer again to steady simulations

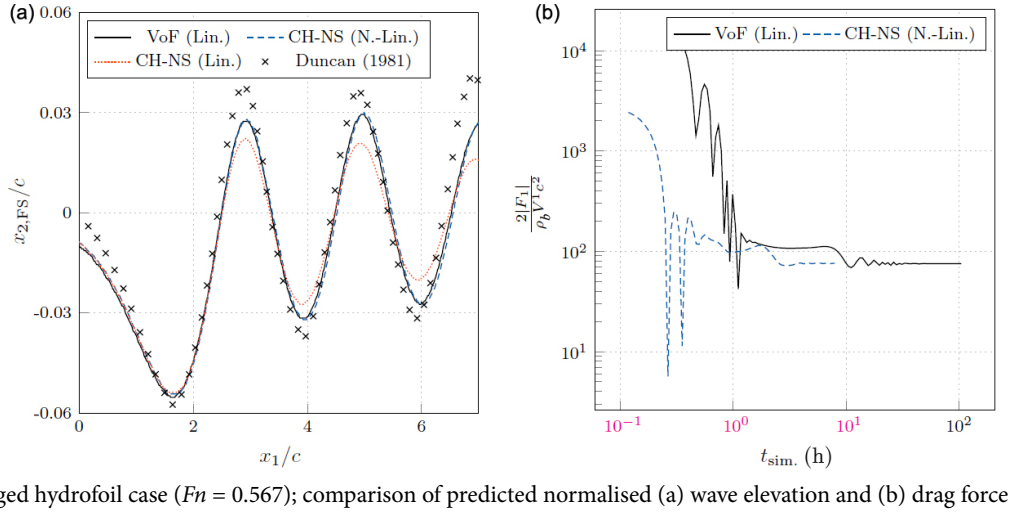

Fig. 9 Submerged hydrofoil case (Fn = 0.567); comparison of predicted normalised (a) wave elevation and (b) drag force over wall-clock time.

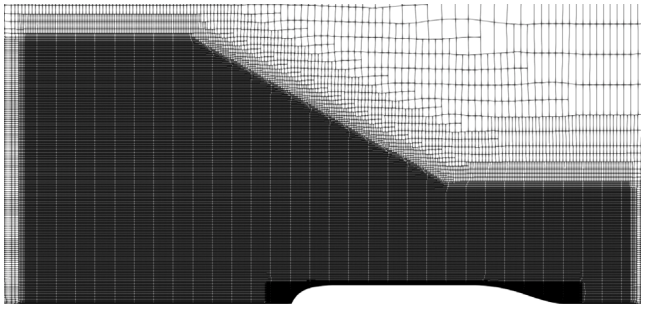

Fig. 10 Illustration of the employed computational mesh along the still water plane in the vicinity of the container ship hull.

using $\tilde{M} = 0.1$ and the non-linear EoS. VoF calculations employ time stepping based on $\delta t = \delta x_{3,\mathrm{FS}} \,/\, VCo_{\delta x}$, where the Courant number is assigned to $Co = 0.3$ and $\delta x_{3,\mathrm{FS}}$ denotes the vertical resolution of the free surface. All simulations are performed until the integrated forces on the hull converge.

Figure 11 depicts the evolution of total resistance over the wall-clock time. The predicted total drag force coefficient is normalized with the static wetted surface of 9.5121 m^2 and converges to $C_T = 3.68\times10^{-3}$ and $C_T = 3.66\times10^{-3}$ for the CH-NS and the VoF simulation. Detailed qualitative and quantitative CPU-efforts are given in Table 2. Both values differ by only 0.5% and compare favourable with the experimental value $C_T = 3.56\times10^{-3}$ —subject to the influence of other aspects, e.g., turbulence modelling. However, the CH-NS approach clearly outperforms the VoF simulation with respect to computational time, while introducing only minor additional wave damping, cf. Fig. 12. The wave elevation ($x_{\mathrm{FS},3} \,/\, L_{pp}$) measured at three different lateral planes through the free surface, i.e., $x_2 \,/\, L_{pp} = 0.0741$, $x_2 \,/\, L_{pp} = 0.1509$, and $x_2 \,/\, L_{pp} = 0.4224$, is compared with experimental data in Fig. 13. The predictive discrepancy is generally small and the non-linear CH-NS tends to provide slightly larger amplitudes. Mind that the non-linear EoS (10) leads to a significant sharpening of the density field, as illustrated by Fig. 14.

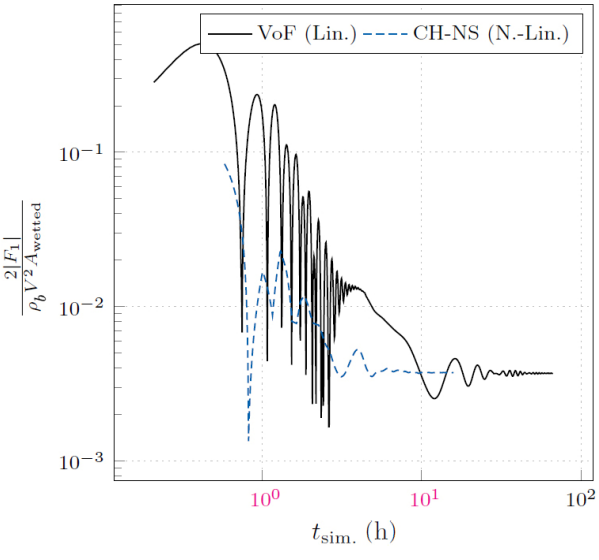

Fig. 11 Evolution of the predicted drag force over the wall-clock simulation time for the VoF and CH-NS simulation of the container vessel at $Re = 1.4\times10^7$ and $Fn = 0.26$.

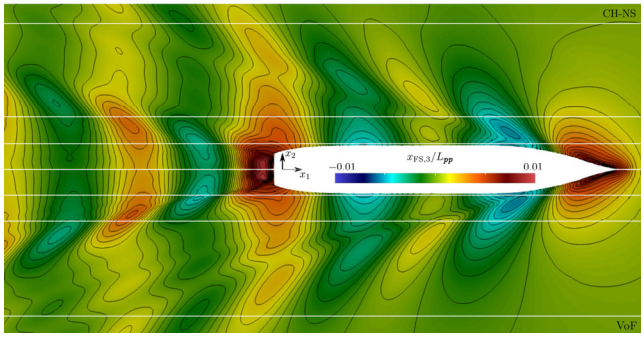

Fig. 12 Comparison of predicted wave field around the Kriso container vessel at $Re = 1.4\times10^7$ and $Fn = 0.26$ obtained by the VoF (bottom) and CH-NS (top) approach. White horizontal lines indicate evaluation planes used for the wave cuts displayed in Fig. 13.

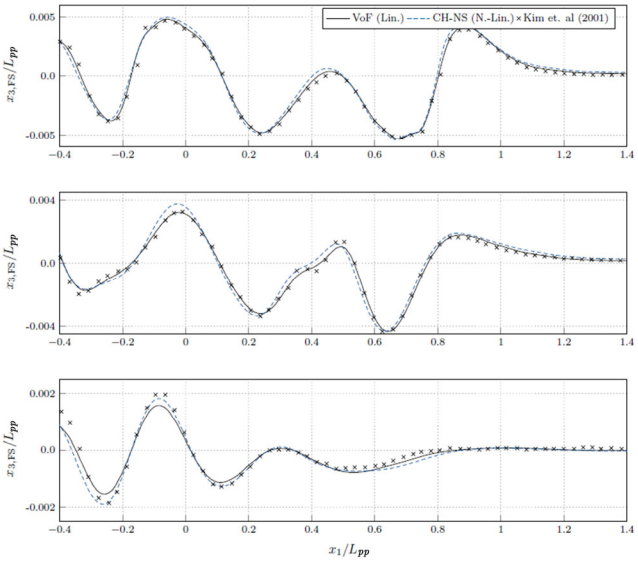

Fig. 13 Comparison of measured and predicted wave elevation in 3 lateral planes, i.e., close to the hull at (a) $x_2 \,/\, L_{pp} = 0.0741$, (b) at $x_2 \,/\, L_{pp} = 0.1509$, and at a remote position (c) $x_2 \,/\, L_{pp} = 0.4224$.

7 Discussion and outlook

The paper presents an alternative approach for the simulation of marine free surface flows at engineering scale. The method (labelled CH-NS) can be displayed as a Volume-of-Fluid (VoF) approach which is extended by a diffusive right hand side of order four obtained from a Cahn-Hilliard (CH) system. While the CH-framework is often used to describe phase separation processes along diffuse interfaces, the phase

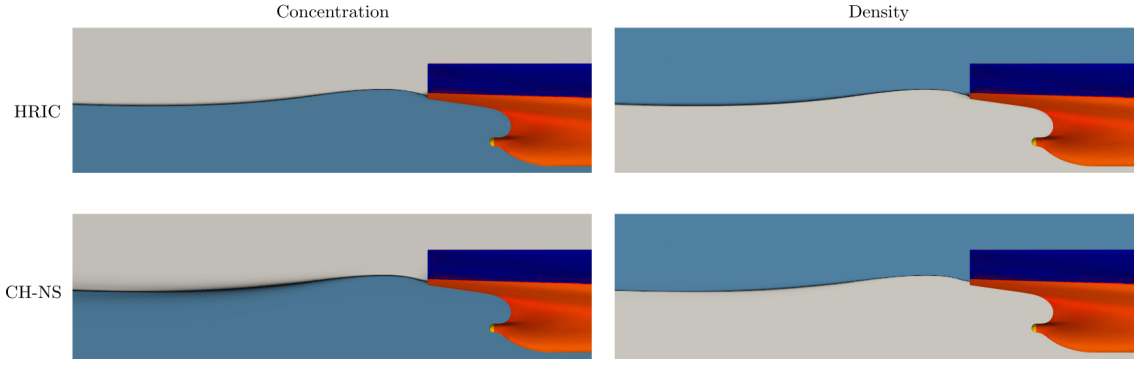

Fig. 14 Concentration (left) and density field (right) obtained from a VoF with linear EoS (top) and a CH-NS with non-linear EoS (bottom).

transition region usually falls below the typical grid resolution in engineering settings. Therefore these settings closely resemble the sharp interface limit.

The phase separating characteristics of the CH-NS system is supported by negative diffusivity of the concentration equation in the central transition regime. This involves $\approx 60\%$ negative diffusion for the double-well potential used in this paper, and scales with the mobility. A spatially homogeneous but temporally/iteratively variable mobility, adapted to an error expression, is suggested. This leads to robust results—based on traditional upwind biased convective approximations—with a fair predictive accuracy and resharpening capabilites. The model involves a free parameter which is assigned to a value well below the stability limit. An alternative non-linear material law is supplementary used to improve minimal blurring.

The implementation of the CH-NS system was verified for an analytical laminar Couette flow. Subsequently, different laminar and turbulent two-phase flows were used to validate the results against experimental or theoretical data, reaching from the capillary to the gravity scale. The CH-NS approach naturally includes surface tension effects but the more relevant advantages refer to the efficiency and the resharpening capability of the approach. Unlike a VoF approach, accurate steady simulations can be performed much faster without any CFL-constraint, since the volume- or mass fraction equation turns into a classical convection-diffusion equation. The latter makes use of taylored, compressive convection schemes obsolet and supports the use of upwind biased approximation of convective kinematics.

Efficiency benefits over the traditional VoF method were demonstrated for a fully turbulent two-phase flow around a container ship hull at realistic Froude- and large Reynolds-numbers in steady state. For all cases presented in this paper, the computational time is reduced by at least one order of magnitude and minor predictive differences were observed in comparison with the VoF method.

Appendix

A.1 Stability analysis

A discrete von-Neumann stability analysis of Eq. (38) yields the following amplification factor:

$$\xi = \frac{\xi^{m+1}}{\xi^{m}} = \frac{1 + Co^{\mathrm{diff}} \frac{C_2}{C_1 \delta x^2}\left[4\cos^2(\varphi) - 8\cos(\varphi) + 5\right]}{1 + Co\left[1 - \cos(\varphi) + i\sin(\varphi)\right] + 2Co^{\mathrm{diff}} b''\left[1 - \cos(\varphi)\right]} \tag{42}$$

Here i and m represent the complex constant ($i^2 = -1$) and an iteration counter, and the parameter $\varphi = \beta\delta x$ with $\cos(\beta\delta x) = 1/2(\mathrm{e}^{-I\beta\delta x} + \mathrm{e}^{I\beta\delta x})$ represents the phase angle. The system can be thought of as unconditional stable if $\xi \leq 1$. With attention restricted to the under-resolved situation ($C_1 = 1$ Pa, $C_2 = 0$ N), we obtain

$$\begin{aligned}\xi = \frac{\xi^{m+1}}{\xi^{m}} &= \frac{1}{1 + \left(Co + 2Co^{\mathrm{diff}} b''\right)\left[1 - \cos(\varphi)\right] + iCo\sin(\varphi)} \\ &= \frac{1 + \left(Co + 2Co^{\mathrm{diff}} b''\right)\left(1 - \cos(\varphi)\right)}{\left[1 + \left(Co + 2Co^{\mathrm{diff}} b''\right)\left(1 - \cos(\varphi)\right)\right]^2 + \left(Co\sin(\varphi)\right)^2} \\ &\quad - i\frac{Co\sin(\varphi)}{\left[1 + \left(Co + 2Co^{\mathrm{diff}} b''\right)\left(1 - \cos(\varphi)\right)\right]^2 + \left(Co\sin(\varphi)\right)^2}\end{aligned} \tag{43}$$

Confining the interest to the real term in Eq. (43), the system is stable for the pure phases ($c_0 = 0$, $c_0 = 1$). Along the phase transition regime $c = 0.5$ we estimate the stability limits by

$$\tilde{M} \leq 1 \quad \text{and} \quad \tilde{M} \geq 1 + \frac{2}{Co\left(1 - \cos(\varphi)\right)} \tag{44}$$

Figure 15 depicts the amplification factor for three different Courant numbers ($Co = 0.1$, $Co = 1$, $Co = 10$) and five different exemplary phase angles as a function of the non-dimensional mobility parameter $\tilde{M}$.

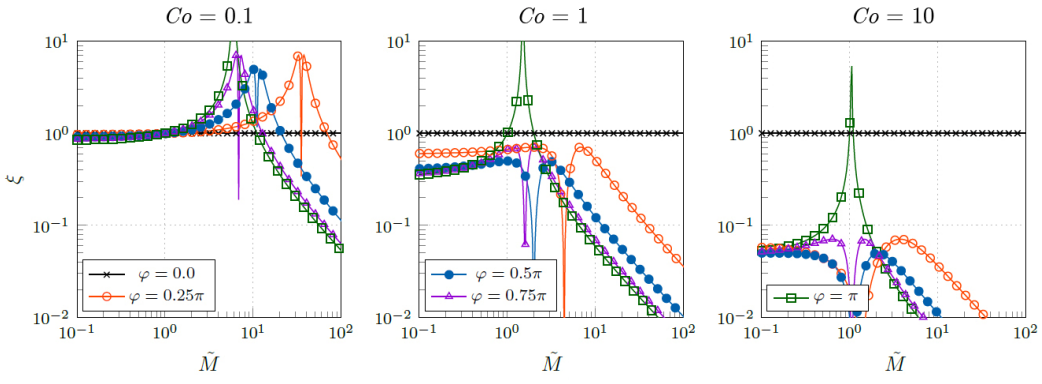

Fig. 15 Amplification factor of a one dimensional CH-NS system over the mobility factor $\tilde{M}$ for different phase angles φ and Courant-numbers, i.e., $Co = 0.1$ (left), $Co = 1$ (middle), and $Co = 10$ (right).

A.2 Computational time

Table 2 Measured CPU efforts for 2D and 3D turbulent multi-phase simulations

Case	Method	n_{CPU}	t_{CPU} (h)
2D-Hydrofoil	VoF	4	494.60
	CH	4	34.32
	Ratio	1	14.14
3D-Ship	VoF	960	37814.43
	CH	960	8428.8
	Ratio	1	4.47

Acknowledgements

The current work is a part of the research projects "Drag Optimisation of Ship Shapes" funded by the German Research Foundation (DFG, Grant No. RU 1575/3-1) as well as "Dynamic Adaptation of Modular Shape Optimization Processes" funded by the German Federal Ministry for Economic Affairs and Energy (BMWi, Grant No. 03SX453B). This support is gratefully acknowledged by the authors. Selected computations were performed with resources provided by the North-German Supercomputing Alliance (HLRN). In addition, we would like to mention the Matlab Symbolic Toolbox (The MathWorks, 2019), which was a great help when calculating the analytical solutions.

Funding note

Open Access funding enabled and organized by Projekt DEAL.

Declaration of competing interest

The authors have no competing interests to declare that are relevant to the content of this article.

References

Abels, H., Garcke, H., Grün, G. 2012. Thermodynamically consistent, frame indifferent diffuse interface models for incompressible two-phase flows with different densities. *Math Mod Meth Appl S*, 22: 1150013.

Banks, J., Phillips, A., Turnock, S. R. 2010. Free surface CFD prediction of components of ship resistance for KCS. In: Proceedings of the 13th Numerical Towing Tank Symposium.

Brackbill, J. U., Kothe, D. B., Zemach, C. 1992. A continuum method for modeling surface tension. *J Comput Phys*, 100: 335–354.

Cahn, J. W., Hilliard, J. E. 1958. Free energy of a nonuniform system. I. Interfacial free energy. *J Chem Phys*, 28: 258–267.

Ding, H., Spelt, P. D. M., Shu, C. 2007. Diffuse interface model for incompressible two-phase flows with large density ratios. *J Comput Phys*, 226: 2078–2095.

Duncan, J. H. 1981. An experimental investigation of breaking waves produced by a towed hydrofoil. *Proc R Soc Lond A*, 377: 331–348.

Duncan, J. H. 1983. The breaking and non-breaking wave resistance of a two-dimensional hydrofoil. *J Fluid Mech*, 126: 507–520.

Ferziger, J. H., Perić, M. 2012. *Computational Methods for Fluid Dynamics*. Berlin, Heidelberg: Springer Berlin Heidelberg.

Heyns, J. A., Malan, A. G., Harms, T. M., Oxtoby, O. F. 2013. Development of a compressive surface capturing formulation for modelling free-surface flow by using the volume-of-fluid approach. *Int J Numer Meth Fluids*, 71: 788–804.

Hirt, C. W., Nichols, B. D. 1981. Volume of fluid (VOF) method for the dynamics of free boundaries. *J Comput Phys*, 39: 201–225.

Hohenberg, P. C., Halperin, B. I. 1977. Theory of dynamic critical phenomena. *Rev Mod Phys*, 49: 435.

Jacqmin, D. 1999. Calculation of two-phase Navier-Stokes flows using phase-field modeling. *J Comput Phys*, 155: 96–127.

Jacqmin, D. 2000. Contact-line dynamics of a diffuse fluid interface. *J Fluid Mech*, 402: 57–88.

Jasak, H., Weller, H. G., Gosman, A. D. 1999. High resolution NVD differencing scheme for arbitrarily unstructured meshes. *Int J Numer Meth Fluids*, 31: 431–449.

Khanwale, M. A., Lofquist, A. D., Sundar, H., Rossmanith, J. A., Ganapathysubramanian, B. 2020a. Simulating two-phase flows

with thermodynamically consistent energy stable Cahn-Hilliard Navier-Stokes equations on parallel adaptive octree based meshes. *J Comput Phys*, 419: 109674.

Khanwale, M. A., Saurabh, K., Fernando, M., Calo, V. M., Ganapathysubramanian, B. 2020b. A fully-coupled framework for solving Cahn-Hilliard Navier-Stokes equations: Second-order, energy-stable numerical methods on adaptive octree based meshes. *arXiv preprint* arXiv:2009.06628.

Kim, W. J., Van, S. H., Kim, D. H. 2001. Measurement of flows around modern commercial ship models. *Exp Fluids*, 31: 567–578.

Kröger, J. 2016. A numerical process for the hydrodynamic optimisation of ships. Ph.D. Thesis. Hamburg University of Technology.

Kröger, J., Kühl, N., Rung, T. 2018. Adjoint volume-of-fluid approaches for the hydrodynamic optimisation of ships. *Ship Tech Res*, 65: 47–68.

Kröger, J., Rung, T. 2015. CAD-free hydrodynamic optimisation using consistent kernel-based sensitivity filtering. *Ship Tech Res*, 62: 111–130.

Lafaurie, B., Nardone, C., Scardovelli, R., Zaleski, S., Zanetti, G. 1994. Modelling merging and fragmentation in multiphase flows with SURFER. *J Comput Phys*, 113: 134–147.

Larsson, L., Stern, F., Visonneau, M. 2010. Gothenburg 2010, a workshop on numerical ship hydrodynamics. Department of Shipping and Marine Technology, Chalmers University of Technology, no: R-10:222.

Lowengrub, J., Truskinovsky, L. 1998. Quasi-incompressible Cahn–Hilliard fluids and topological transitions. *Proc R Soc Lond A*, 454: 2617–2654.

Luo-Theilen, X., Rung, T. 2017. Computation of mechanically coupled bodies in a seaway. *Ship Tech Res*, 64: 129–143.

Magaletti, F., Picano, F., Chinappi, M., Marino, L., Casciola, C. M. 2013. The sharp-interface limit of the Cahn–Hilliard/Navier–Stokes model for binary fluids. *J Fluid Mech*, 714: 95–126.

Manzke, M., Voss, J. P., Rung, T. 2013. Sub-cycling strategies for maritime two-phase flow simulations. In: *Recent Developments in the Numerics of Nonlinear Hyperbolic Conservation Laws. Notes on Numerical Fluid Mechanics and Multidisciplinary Design, Vol. 120*. Ansorge, R., Bijl, H., Meister, A., Sonar, T. Eds. Springer Berlin Heidelberg: 237–251.

Menter, F. R., Kuntz, M., Langtry, R. 2003. Ten years of industrial experience with the SST turbulence model. *Turbulence, Heat and Mass Transfer*, 4: 625–632.

Muzaferija, S., Peric, M. 1999. Computation of free-surface flows using interface tracking and interface-capturing methods. In: *Nonlinear Water Wave Interaction*. Wessex Institute of Technology Press: 59–100.

Noh, W. F., Woodward, P. 1976. SLIC (simple line interface calculation). In: Proceedings of the 5th International Conference on Numerical Methods in Fluid Dynamics: 330–340.

Olsson, E., Kreiss, G. 2005. A conservative level set method for two phase flow. *J Comput Phys*, 210: 225–246.

Olsson, E., Kreiss, G., Zahedi, S. 2007. A conservative level set method for two phase flow II. *J Comput Phys*, 225: 785–807.

Osher, S., Sethian, J. A. 1988. Fronts propagating with curvature-dependent speed: Algorithms based on Hamilton-Jacobi formulations. *J Comput Phys*, 79: 12–49.

Pilliod, J. E. Jr., Puckett, E. G. Jr. 2004. Second-order accurate volume-of-fluid algorithms for tracking material interfaces. *J Comput Phys*, 199: 465–502.

Prosperetti, A. 1981. Motion of two superposed viscous fluids. *Phys Fluids*, 24: 1217–1223.

Rider, W. J., Kothe, D. B. 1998. Reconstructing volume tracking. *J Comput Phys*, 141: 112–152.

Rung, T., Wöckner, K., Manzke, M., Brunswig, J., Ulrich, C., Stück, A. 2009. Challenges and perspectives for maritime CFD applications. *Jahrbuch der Schiffbautechnischen Gesellschaft*, 103: 127–39.

So, K. K., Hu, X. Y., Adams, N. A. 2011. Anti-diffusion method for interface steepening in two-phase incompressible flow. *J Comput Phys*, 230: 5155–5177.

Song, B., Plana, C., Lopez, J. M., Avila, M. 2019. Phase-field simulation of core-annular pipe flow. *Int J Multiphase Flow*, 117: 14–24.

Sussman, M. 1994. A level set approach for computing solutions to incompressible two-phase flow. Ph.D. Thesis. University of California Los Angeles.

Sussman, M., Fatemi, E., Smereka, P., Osher, S. 1998. An improved level set method for incompressible two-phase flows. *Comput Fluids*, 27: 663–680.

The MathWorks. 2019. Symbolic Math Toolbox. Natick, Massachusetts, United States. Available at https://www.mathworks.com/help/symbolic/.

Ubbink, O., Issa, R. I. 1999. A method for capturing sharp fluid interfaces on arbitrary meshes. *J Comput Phys*, 153: 26–50.

Völkner, S., Brunswig, J., Rung, T. 2017. Analysis of non-conservative interpolation techniques in overset grid finite-volume methods. *Comput Fluids*, 148: 39–55.

Wackers, J., Koren, B., Raven, H. C., van der Ploeg, A., Starke, A. R., Deng, G. B., Queutey, P., Visonneau, M., Hino, T., Ohashi, K. 2011. Free-surface viscous flow solution methods for ship hydrodynamics. *Arch Computat Methods Eng*, 18: 1–41.

Wilcox, D. C. 1998. *Turbulence Modeling for CFD, Vol. 2*. DCW Industries La Canada.

Yakubov, S., Cankurt, B., Abdel-Maksoud, M., Rung, T. 2013. Hybrid MPI/OpenMP parallelization of an Euler-Lagrange approach to cavitation modelling. *Comput Fluids*, 80: 365–371.

Yakubov, S., Maquil, T., Rung, T. 2015. Experience using pressure-based CFD methods for Euler-Euler simulations of cavitating flows. *Comput Fluids*, 111: 91–104.